IEEE Robotics and Automation Letters (RA-L) paper, presented at ICRA 2026, Vienna, Austria. Cite as RA-L paper.

High-Velocity, Pressure-Driven Eversion for Rapid Vine Robots

Anna Alvarez[1*], Anders Seawright[1], Neel Tripathi[1], Carlos Cruz[2], Selena Deng[1], and Elliot W. Hawkes[1]

***Abstract*—"Vine robots" are thin-walled, tubular, pneumatic soft robots that lengthen at their tips to navigate constrained and complex environments. Previous studies have already explored the mechanics of vine robot bodies and investigated applications for which the device is well-suited. However, these studies almost exclusively focus on eversion rates in the quasi-static regime, overlooking other potential applications of high-speed vine robots in medical devices, projectile launchers, or for informing biology. To better understand this rapid behavior, we present a dynamic growth model for high-velocity vine robot body extension with a payload mass and verify the model experimentally. To the best of the authors' knowledge, this is the first instance of vine robots utilized for projectile launching. We find three key results: i) vine robot bodies experience rate-dependent damping that is scale-dependent and monotonically increases with increasing wall thickness; ii) steady-state velocity, or the upper limit of speed in terms of growth velocity, monotonically increases with isometric scaling; and iii) energy efficiency increases with decreasing wall thickness. These findings are used to inform the preliminary design of a large-scale, drug delivery device proof-of-concept, as well as design the fastest–on–record vine, capable of 60 m/s eversion. Our work provides a basic understanding of the dynamic movement of vine robots and opens the door to new areas of application.**

I. Introduction

There exists an emerging class of shape-changing robots that utilize extension from the tip, or "growth," as a navigation strategy. These thin-walled, tubular robots are inspired by a variety of tip-extending organisms in biology, including pollen tube growth [1], fungal hyphae [2], and nerve cells of animals [3]. In these cases, localized growth is achieved by the addition of material onto the tip, allowing for the rest of the body to remain stationary. By removing the need to slide across the ground for environmental navigation, tip growth reduces skin friction experienced by the body. Robots that employ this strategy of continuous, additive growth from the tip utilize techniques such as additive manufacturing of thermoplastic filament [4], local photo-polymerization [5], or a combination of fiberglass thread with UV curing [6]. Despite these robots growing orders of magnitude faster (cm/min) than their biological counterparts (cm/day), their growth is still relatively slow due to the extrusion or curing time.

Manuscript received: January, 31, 2025; Revised: May, 21, 2025; Accepted: July, 2, 2025.

This paper was recommended for publication by Editor Yong-Lae Park upon evaluation of the Associate Editor and Reviewers' comments. This work was supported by the NSF (grant no. 1944816).

[1]Anna Alvarez, Anders Seawright, Neel Tripathi, Selena Deng, and Elliot W. Hawkes are with the Department of Mechanical Engineering, University of California, Santa Barbara, CA 93106, USA anna_alvarez@ucsb.edu

[2]Carlos Cruz is with the Department of Physics, University of California, Santa Barbara, CA 93106, USA

Digital Object Identifier (DOI): see top of this page.

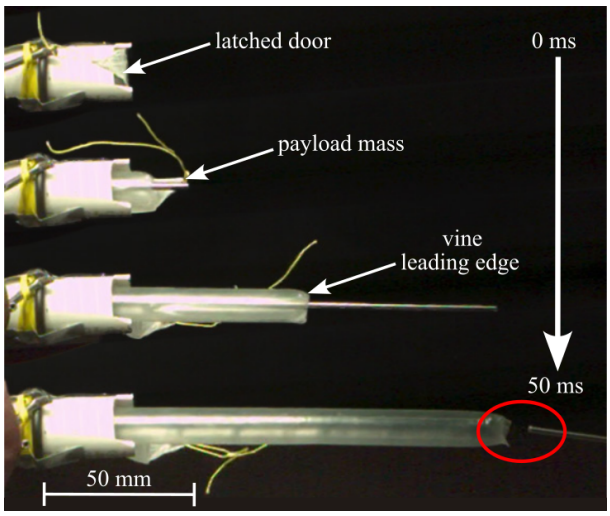

Fig. 1. Time lapse of a high-speed vine robot body eversion while carrying a payload mass. The release of a latched door allows for eversion to begin. At 50 ms, the payload mass is ballistically ejected from the vine robot body. The maximum velocity recorded across all vine robot bodies was 60 m/s.

Vine robots are a subclass of tip-extending robots that utilize eversion and are characterized by thin-walled tubular bodies [7] [8]. During eversion, the material on the inside of the body is flipped outward to then become an external structure, as seen in Fig. 1. The soft nature of the material allows the vine body to passively conform to its environment. With the addition of controls, sensors, and steering capabilities, vine robots have been used for archaeological exploration [9], burrowing through granular media [10], and are being developed for endovascular surgery [11]. The phenomena of eversion is found in various biological examples such as the branched proboscis of ribbon worms [12] and at the micron-scale, penetrating stylets of jellyfish stinging cells (nematocyst tubules) [13]. These biological eversion examples occur on time scales orders of magnitude faster than the biological growth examples. For example, the nematocyst stinging organelles of cnidarians—such as jellyfish and sea anemones—evert tubules at 2.7 - 37.1 m/s [14]. Despite the high accelerations seen in nature and the known ability of vine robots to evert at high speeds with increased driving pressure, current vine robots are nearly all used in the quasi-static regime. Two exceptions involve demonstrations at relatively high leading edge extension speeds of 4 m/s [10] and 10 m/s [15] [7], but neither work studies the dynamics of high-velocity movements. As such, there is a lack of fundamental understanding of high-velocity and high-acceleration movements in vine robots.

The following paper offers three primary contributions. First, we present a dynamic growth model for high-speed vine robot bodies that carry and ballistically eject a payload

IEEE Robotics and Automation Letters (RA-L) paper, presented at ICRA 2026, Vienna, Austria. Cite as RA-L paper.

mass using pressurized air. Second, we demonstrate a vine robot launching a projectile, which to the best of the authors' knowledge, is the first instance of this behavior. Third, we design and test a vine robot capable of everting at 60 m/s, which to the best of the authors' knowledge, is the fastest on record.

The presented dynamic vine robot growth model informs robotic design and can be used to understand biological eversion and the effects of relevant parameters. This is particularly helpful in cases where direct measurement of these specimens is a challenge due to short time frames and small length scales during eversion, such as in micron-scale nematocysts. Additionally, a basic understanding and demonstration of dynamic vine robot eversion and particle ejection opens the door to new application areas such as drug delivery, projectile launchers, proboscis-inspired "prey" capture, rapidly deploying fall cushioning, or medical devices that move quickly in order to, for example, actively track heart motions during ablation surgery. One such application of high-speed everting vine robots explored herein is micron-scale dynamic vines for transdermal drug delivery, inspired by jellyfish nematocysts. The creation of a jellyfish-inspired stinger will act as an alternative active method to penetrate the topmost layer of the skin without the use of hypodermic needles [16].

The subsequent section of this paper presents a second-order differential equation that captures the dynamics of fast vine robot eversion. The next section outlines experimental results, which show the following: a near-linear relationship between the damping term and scale; a steady-state velocity which monotonically increases with scale, and an improved vine energy efficiency with decreasing thickness. Finally, we demonstrate the potential for eventual real-world applications by designing and fabricating a large-scale model of a device that can eject payloads, laying the groundwork for future transdermal drug delivery devices.

II. Modeling

The following section presents a model for dynamic vine robot eversion. As outlined in Fig. 2, the eversion process involves pressurizing gas into a thin–walled tube, forcing the internal structure–the "tail" of the vine robot body–to be pulled through the core of the body and turn inside-out. Unique to this work, the tail can also carry a payload mass, which is ballistically ejected during high-speed eversion. In previous work, detailed models of quasi-static extension of vine robots have been presented [7], as well as models that account for dynamic oscillations of a cantilevered vine robot after it has been extended into place [17]. However, an analytical dynamic model of rapid eversion is missing from the literature. For the remainder of the paper, we will refer to the vine robot body without additional sensors as just the vine.

For our model, we assume that the acceleration of the vine tail is driven by two forces (a pressure-based force and a gravitational force) and is resisted by five forces. This is represented by the following inhomogeneous nonlinear second-order differential equation:

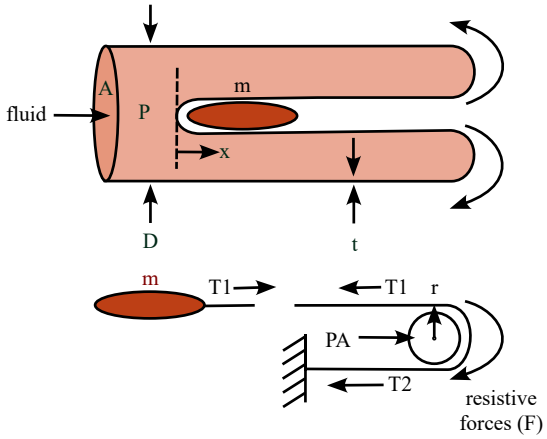

Fig. 2. Schematic of the basic everting vine body concept, with parameters of interest labeled. The left inlet with area A allows for pressurized fluid with pressure P to enter on the left. The red represents the payload mass. The bottom figure is a free body diagram of an eversion pulley model, and outlines the relationship between driving pressure and tension applied on the payload. $T_1 = 1/2PA$ and F encompasses all other loss terms on the right side of Eq. (1).

$$m(x)\ddot{x} = \frac{1}{2}PA + m(x)g - \frac{1}{2}B\dot{x}^n - \frac{1}{2}P_yA - \frac{1}{2}\rho AC_D\dot{x}^2 - \mu_s wL - \sum_i Ce^{\frac{\mu_c L_i}{R_{ci}}} \quad (1)$$

We define x to be the position of the vine tail, m is the combined payload mass and vine mass, P is the internal gauge pressure, g is the gravitational constant, A is the vine cross-sectional area, B is a damping coefficient, n is a damping exponent, P_y is the yield pressure, ρ is the surrounding fluid's density, C_D is the drag coefficient, w is the normal force between the vine tail and body per unit length, L is the vine body length, μ_s is the friction coefficient between the vine tail and the vine body's internal surface when the vine is straight, μ_c is the friction coefficient between the vine tail and body when the vine is curved, C is a constant correlating to the input tension of capstan friction, and R_c is the radius of curvature.

The inertial term (on the left-hand side) includes a length-dependent term, $m(x) = m_{vine} + m_{pay} - cx$, where m_{vine} is the vine mass, m_{pay} is the payload mass, and c is the linear density of the vine. The tail mass decreases during growth, given that the tail shortens as eversion progresses; this assumes the vine tail is equal to the length of the vine body to start, and not on a reel as in some instantiations of vine robots. The speed at which the tail length decreases is twice the speed of vine extension.

The first term on the right-hand side is the pressure-based driving force. The coefficient of $1/2$ can be explained through a model of the vine cross-section as a pulley system (Fig. 2). The forces include tension on either side of the pulley system (T_1 and T_2), and the combination of viscous rate-dependent and Coulomb-like rate-independent forces (F). Using static force balance of torques and forces, it is found that $PA = T_1 + T_2$ and $rT_1 + rF = rT_2$ where r is the pulley radius. Tension on the payload mass is equivalent to $T_1 = \frac{PA-F}{2}$, resulting in a coefficient of $1/2$ being attached to both the driving pressure

IEEE Robotics and Automation Letters (RA-L) paper, presented at ICRA 2026, Vienna, Austria. Cite as RA-L paper.

(first term) and the resistive, path-independent forces (third and fourth terms).

The second term on the right-hand side is the gravitational force. This term is dependent on the direction of vine eversion, and currently represents a vine everting downwards with the aid of gravity.

The third term on the right-hand side is the rate-dependent eversion force. This force likely arises from the combination of multiple complicated physical phenomena, including skin buckling, wrinkling, and nonlinear viscoelasticity from the material [18], making the term difficult to derive from first principles. Therefore, a simpler approach is taken in this work by fitting an exponential model. In the pulley model, this term is analogous to a damping term in the bearing of the pulley.

The fourth term is the rate-independent eversion force, or the quasi-static yield force. This force is dependent of the yield pressure–the threshold pressure required to begin vine tip eversion. In the pulley model, this term is analogous to a Coulomb friction force in the bearing of the pulley.

The fifth term is the air drag experienced by the head of the vine. The air drag term can be important for dynamic eversion in cases of high velocity. However, we ignore the drag force when the combination of driving pressure and tail velocity results in drag less than approximately 5% of the driving force. For example, in a 50 μm thick, 150 mm long vine with a 24 mm diameter, the drag force does not exceed this threshold until 56 kPa, assuming a drag coefficient of 0.82 for a cylindrical rod. All experimental tests produced a drag force of approximately 5% or below, allowing the term to be ignored, except for the 60 m/s vine.

The sixth and seventh terms are the length-dependent friction term and the curvature-based friction term. This sixth term is small for relatively short (< 30 cm) vines, and this seventh term is small for relatively straight ($< 30^\circ$ curvature) vines [7]. Given that the vines considered in this work are straight and short, we neglect these terms.

With the fifth, sixth, and seventh terms assumed to be negligible, we can rearrange the remaining terms into a simplified form:

$$m\ddot{x} + \frac{1}{2}B\dot{x}^n = \frac{1}{2}(P - P_y)A + m(x)g \tag{2}$$

To explore the speed limits of these systems, we examine the case where the forces are balanced and the acceleration is zero. We also assume that payload mass is zero, such that the gravitational force is much smaller than the driving force and can be ignored. In this scenario, the velocity reaches a steady-state, $\dot{x}_{ss}$, meaning the system has reached its maximum speed for the given pressure. The force required to reach this velocity can be expressed as shown in Eq. 3.

$$(P - P_y)A = B\dot{x}_{ss}^n \tag{3}$$

Measured values of pressure, area, and steady-state velocity can be used to calculate the coefficient B and n for a given vine.

III. Methods and Experimental Design

In this section, we provide an overview of the fabrication of vine bodies, the experimental setup required for filming and everting high-speed bodies, the testing procedures, and the data analysis used.

A. Fabrication

To validate our model (Eq. 2) and to better understand the behavior of rapidly everting vines, we tested an assortment of vine bodies of varying diameter, thickness, and payload. Key requirements for these vine bodies are that they must be airtight, withstand a wide range of driving pressures without bursting, and be easily and reliably reproducible. To meet these requirements, we adapted a previously established two-step manufacturing process [19].

First, the vine body was made by heat sealing two identical sheets of 90A Thermoplastic Polyurethane (TPU) together on a Fancierstudio Digital Heat Press for two minutes. Heat sealing kept the sheets flush together, and temperatures were chosen such that the sheets were not permanently bonded together. Next, the layered TPU sheets were laid flat and adhered to the Trotec Speedy 100 laser cutter bed via masking tape. This prevented the film from shifting or warping during the cutting process. The laser cutter's purpose is twofold. First, it was used to cut out the desired geometry–rectangles with widths equivalent to half the circumference. Second, the laser welds the TPU sheets on contact, creating an airtight seal around the vine. It is important to tune the laser power and speed to prevent the TPU from melting significantly or from being too cool and leaving un–welded gaps along the seam. Both the heat press and laser cutter settings for four vine thicknesses were experimentally determined and are listed in Table I.

B. Experimental Setup

There are three key requirements for the test setup built: (1) contain a latching mechanism that allows for fast vine release once the desired pressure has built up, (2) be able to accommodate vine bodies of varying diameters, and (3) allow the vine to evert at a near-constant pressure throughout its extension.

To fulfill the first two requirements, the setup presented in Fig. 3 was built. The setup is comprised of a large working volume, a connector to which a vine is attached, and a lightweight trap door for releasing the vine. Similar to the latch-mediated spring actuated (LaMSA) mechanism found in nematocysts, this trap door prevents vine growth until a latch is released, thus fulfilling the first requirement [20]. The door and flexure-based hinge are made out of high-strength, low-weight Dyneema. The low mass prevents large momentum transfer when the door is pushed aside by the everting vine, reducing rotational inertia. The printed connector (Formslabs Tough 2000 Resin) contains an inlet to which the vine body can be adhered. Four different connectors were printed with varying inlet diameters to accommodate the range of vine sizes tested, thus fulfilling the second requirement.

To fulfill the final requirement, the internal pressure before and after release, P_1 and P_2, should differ no more than the

IEEE Robotics and Automation Letters (RA-L) paper, presented at ICRA 2026, Vienna, Austria. Cite as RA-L paper.

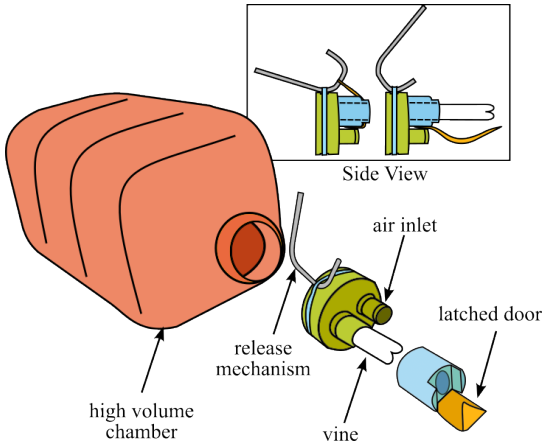

Fig. 3. The experimental setup highlighting the 3.7 liter volume chamber, the release mechanism, the cap adapter containing the air inlet and vine connector, and the latched door. Not illustrated is a pressure gauge and regulator placed prior to the inlet.

selected value of 5% according to $P_2 = \frac{P_1 V_1}{V_2}$. A high-volume chamber of 3.7 liters acts as the initial volume. With the largest vine having a diameter of 24 mm and a length of 280 mm, the maximum volume change is 3.5%, well within the acceptable pressure drop range.

C. Test Samples

In this paper, a combination of four different 90A TPU thicknesses and diameters is tested. We are interested in the effects of isometric scaling on vine performance and therefore created four isometrically scaled vines with dimensions tabulated in Table I. In isometric scaling, R is the scaling factor by which all dimensions are multiplied. We defined the nominal case $R = 1$ to correspond to a thickness of 50 μm and a diameter of 6 mm. Both thickness and diameter are doubled for $R = 2$, quadrupled for $R = 4$, and so on. Isometric scaling isolates size effects on vine growth and allows for generalized predictions on vine performance to be made across sizes.

TABLE I
VINE PARAMETERS FOR DIFFERENT SCALING FACTORS, R.

R	Thick [µm]	Diam [mm]	Heat Press Temp [C^o]	Laser Cutter Power [%]
1	50	6	110	60
2	100	12	82	76
3	150	18	96	81
4	200	24	96	86

D. Test Procedure

Position against time data was collected for each vine body tested. The procedure for doing so is as follows: (1) the open end of the vine body is connected to the air inlet, secured with adhesives and orthodontic rubber bands, and pointed downwards, (2) the air inlet is connected to an external air source, (3) the chamber is pressurized to the desired pressure, (4) the release pin is removed to free the latched door, (5) vine eversion is recorded using a Chronos 2.1-HD High Speed Camera at 1069 fps and illuminated by a Godex SL100D LED video light to improve light exposure, and (6) the position of the vine leading edge is tracked through time using Physics Tracker image analysis software. It is considerably easier to accurately measure the leading edge position compared to the tail position, as the latter is concealed within the vine; we note that the leading edge moves at half of the rate of the tail due to the mechanism of eversion. 4-5 trials are taken for each vine variation.

Data was collected to find the relationship between the steady-state velocity of the tail ($\dot{x}_{ss}$) and the driving force above yield, the effects of R on $\dot{x}_{ss}$, and the relationship between energy efficiency and material thickness. In the first experiment described, four isometrically scaled vines with dimensions found in Table I were grown at 8-11 different pressures with no payload mass. The gauge pressure at which $\dot{x}_{ss}$ was reached was recorded, along with the yield pressures of each vine to calculate the growth force. For the second relationship described, the same four isometrically scaled vines were grown at a pressure of 24 kPa until $\dot{x}_{ss}$ was reached. A total of 4 trials were performed for each vine to determine the average $\dot{x}_{ss}$. Lastly, for energy efficiency tests, 12 mm and 18 mm diameter vines of varying thickness were everted at 34 kPa. Non-steady-state velocities were recorded after vines reach a length of 150 mm, and a heavy payload mass of 35.6 g was used to amplify the inertial effects.

E. Data Analysis

The damping term B is determined by fitting Eq. (3) to the driving force above yield vs. steady-state velocity of the vine tail data. In Eq. (3), $\dot{x}_{ss}$ is a function of the following: B, another fitted term n, the vine cross-sectional area, and pressure above yield. In order to determine the $\dot{x}_{ss}$ for a given pressure, the appropriate vine is grown and the derivative of the leading edge position vs. time data is taken to determine leading edge velocity across time. A time window, which must contain at least three consecutive points, was manually selected on this plot. To be considered steady-state, the coefficient of variation (ratio of the velocity standard deviation to mean velocity) in this window must be below a selected threshold value of 3%. Pressure is increased incrementally until steady-state is achieved for the given vine length. In a log-log plot of driving force across measured $\dot{x}_{ss}$, a best fit power plot of the form $B\dot{x}_{ss}^{n}$ is found using the least squares fit. This power function can be mapped directly to Eq. (3) and is used to calculate B for a given vine geometry.

Lastly, the energy efficiency is determined by dividing kinetic energy output by the pressure–volume work input. The energy output is calculated using the measured, non-steady-state velocity. The energy input is determined using the product of driving pressure and volume change of the vine.

IV. EXPERIMENTAL RESULTS

The following section includes experimental testing results that validate our model, as well as results exploring scaling effects on steady-state velocity, damping, and efficiency. We found three key takeaways. First, when vines are increased in scale isometrically or when material thickness is increased

IEEE Robotics and Automation Letters (RA-L) paper, presented at ICRA 2026, Vienna, Austria. Cite as RA-L paper.

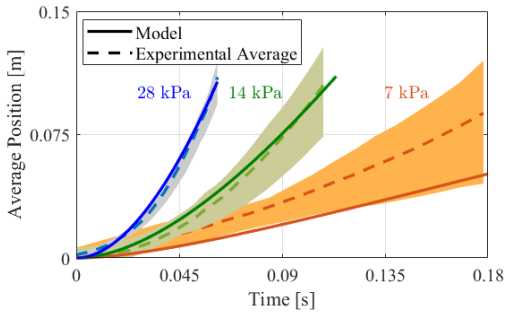

Fig. 4. Model validation using 200 µm thick, 24 mm diameter TPU vines with a 35.6 g payload mass. The dotted lines represent the average of four runs, while the solid line represents the model estimate. N=4.

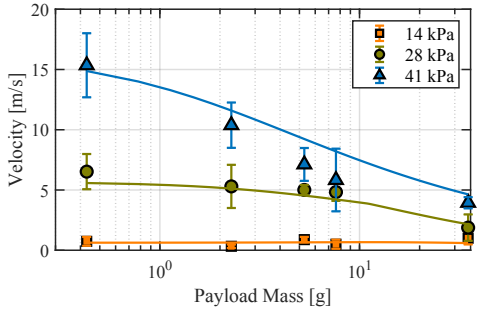

Fig. 5. A comparison of predicted velocities and experimental velocities for 24 mm diameter vines after 12 cm of eversion. Experimental results are represented by symbols, and predicted results are represented by lines. All vines used TPU of 150 µm in thickness. N=4.

while diameter is held constant, the damping term monotonically increases. Second, the steady-state velocity increases monotonically with isometric scaling. Third, the efficiency increases with decreasing thickness.

A. Model Validation

Our model in Eq. (2) predicts the position of the vine payload mass versus time with an error of 0.3 cm for high pressures and 1.9 cm for lower pressures. Fig. 4 presents a comparison between our experimental results and our prediction of position vs. time of the vine leading edge for 3 different pressures (7, 14, and 28 kPa). The following tests are for a 25 mm diameter TPU vine of 200 µm wall thickness with a payload mass of 35.6 g. Material effects dominate when growth pressures are closer to yield pressure (3 kPA), resulting in a decrease in the accuracy of the model. The root mean square (RMS) error of our model prediction is included in the second column of Table II. The model was further validated by comparing experimental vs. theoretical final vine velocity against payload mass for three driving pressures (14, 28, and 41 kPa) as seen in Fig. 5. These tests were done on a vine with 150 µm wall thickness, and the RMS [m/s] error values are included in the third column of Table II.

TABLE II
RMS ERROR BETWEEN EXPERIMENTAL AND SIMULATED VALUES

Pressure [*kPa*]	Position RMS [*cm*]	Velocity RMS [*m*/*s*]
7	1.90	NA
14	0.29	0.27
28	0.31	0.56
41	NA	1.35

B. Damping Term is Scale and Thickness Dependent

In order to reduce the damping term $\frac{1}{2}B\dot{x}^n$ from Eq. (2), the vine can be isometrically scaled down, or vine wall thickness can be decreased. As was presented in the Methods section, the B and n coefficients are fitted terms from Fig. 6. Using a least squares fit, the n value that approximates all four scales is 0.37. The power function coefficient, B, is calculated using a least squares fit with the approximation for n. For the scaling factors R = 1, 2, 3, and 4, the statistical measure R^2 is calculated to be 0.964, 0.981, 0.896, and 0.971, respectively.

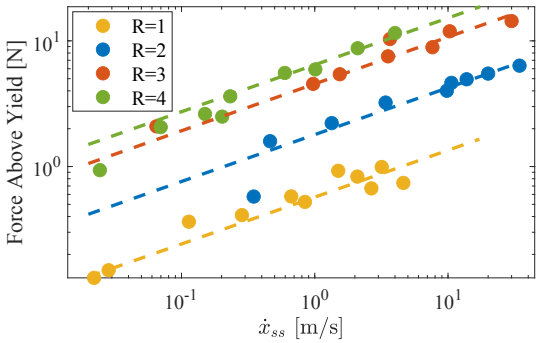

Fig. 6. The growth force above yield required for different steady-state velocities. The dashed line represents a fitted power function with an exponent n of 0.37. As the vine increases in scale, the B value for R =1,2,3,4 is the power coefficient and is calculated to be 0.57, 1.83, 4.54, and 6.44, respectively.

In Fig. 7A, isometric scaling is shown to have a near-linear correlation to the B value. Additionally, Fig. 7B presents the trend between B and thicknesses for vines held at a constant diameter of 12 mm. Given a fixed diameter, the damping term increases linearly with increasing thickness. This matches intuition, as B is associated with the vine material effects.

C. Monotonically Increasing Steady-State Velocity

We next examined how the steady-state velocity changed as a function of scale. We found that the steady-state velocity increases monotonically during isometric scaling, as shown in Fig. 8A, for the range of scales tested. When the steady-state velocity is normalized by vine diameter, no obvious dependence on scale is visible (Fig. 8B). This result suggests that one can achieve higher velocities with larger vines, but this increase in speed is only proportional to the increase in scale. More data is needed to confirm this trend in a wider range of scales.

D. Efficiency of Energy Conversion

To evaluate the performance of the system and to guide future vine design, the input to output energy efficiency of fast vine eversion is reported. Vine energy efficiency improves with thinner wall thicknesses and does not appear to vary with diameter for the range of sizes tested (Fig. 9). The kinetic energy output in these vine eversion tests is calculated from

IEEE Robotics and Automation Letters (RA-L) paper, presented at ICRA 2026, Vienna, Austria. Cite as RA-L paper.

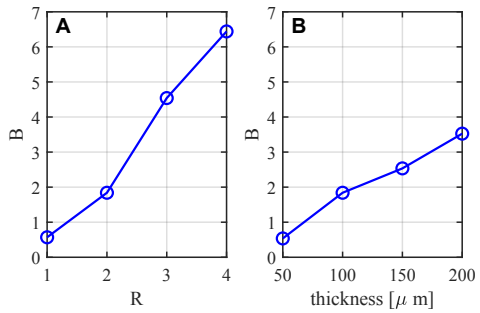

Fig. 7. A) As vines are isometrically scaled, B values increase approximately linearly. B) B values for 12 mm diameter vines with varying thickness. As the thickness increases, B monotonically increases.

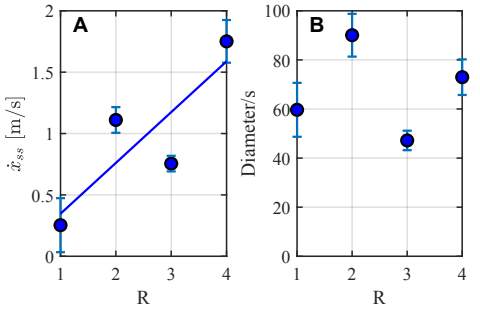

Fig. 8. Steady-state velocity trends for isometrically scaled vines everted at 24 kPa. (A) The best fit linear regression in terms of m/s, where the fitted model results in an $R^2 = 0.935$ and a p-value of 0.32. (B) Tail steady-state velocity normalized by vine diameter.

the measured vine leading edge velocities carrying a payload mass of 35.6 g.

E. High-speed Vine

Using the models and results gathered, a final vine was designed to reach a high velocity, with a target of at least 5 times faster than the 10 m/s shown in previous work [15]. The key parameters that needed to be selected were material thickness, driving pressure, diameter, payload, and length. For material thickness, there is a tradeoff between burst pressure and efficiency. Thicker offers a higher burst pressure, but thinner offers higher efficiency (Fig. 9). Within the thicknesses tested, the best combination of burst pressure and efficiency

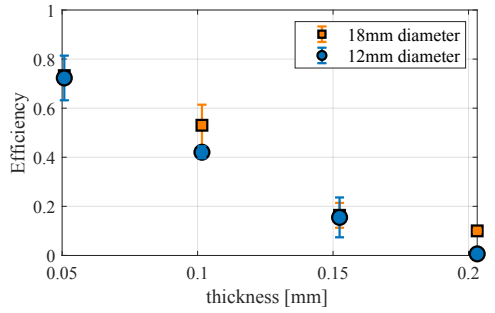

Fig. 9. A representation of the effect of diameter and thickness changes on vine eversion energy efficiency. All vines are grown at 34 kPa with a payload mass of 35.6 g. N=4.

was the 100 μm-thick film. For driving pressure, the higher the value, the faster the eversion (Fig. 4), so it was set to just below the burst pressure (62 kPa). For diameter, increased diameter increases the driving force for a set pressure, and was set to the largest our setup could accommodate (25 mm). For payload, lower masses result in faster speeds (Fig. 6), so a mass of 0 g was chosen. Finally, for length, greater length results in greater time to accelerate, so the maximum length our setup could accommodate was selected (40 cm). The vine constructed reached a leading edge extension velocity of 60 m/s with a predicted velocity of 56 m/s.

V. Transdermal Drug Delivery Proof-of-Concept Prototype

Lastly, we create a macro-scale, transdermal drug delivery (TDD) proof-of-concept prototype to demonstrate a potential application of latchable, high-speed vines. TDD refers to the diffusion of a drug through the skin before circulating through the body [21]. This diffusion can be aided by vehicles, such as microneedles or jet injectors, that perforate the topmost layer of skin [22] [16].

A. Background on TDD

One potential application for the dynamic vines presented above is jellyfish-stinger-inspired devices for injecting medication into the skin. The creation of a jellyfish-inspired stinger will act as an alternative active method to penetrate the topmost layer of the skin and allow for continuous or intermittent drug delivery in the form of a wearable patch. High-velocity vines would be necessary in such an application because the payload mass of a drug must have enough momentum to enter the skin successfully. Other researchers have recognized this potential and have isolated and adapted the stinging cells of cnidaria to deliver drugs [16]. These modified cells demonstrate successful delivery of blue dyes into mouse skin, but are limited to hydrophilic drugs, as the cells still rely on osmotic pressure built up to release. By creating an engineered version of these cells, we can create a TDD device more robust to environmental changes and more tunable to different types of drugs.

B. TDD Device

The device created is a millimeter-scale prototype of a high-speed vine ejector, carrying a payload of colored dye. When the vines penetrate a clear, gelatin-based skin substitute, the dyes diffuse inside. As shown in Fig. 10, this setup is a compact variation of the experimental setup described in Section III. Four separate vines in a 2x2 array are connected to independent high–volume chambers that are pressurized from an external air supply. The pressurized chambers (20 mm in length and 15 mm in diameter) store enough air to propel a 2.5 mm diameter, 12.5 mm long vine with only a 1.7% decrease in pressure during growth. 50 µm thick TPU is used for the vines, and the chamber is 3D printed with Draft V4 resin on a FormLab Form3 printer to ensure a hermetic seal.

Vines are released via a latched door, which consists of engraved, 0.2 mm thick sheets of polystyrene that are held in

IEEE Robotics and Automation Letters (RA-L) paper, presented at ICRA 2026, Vienna, Austria. Cite as RA-L paper.

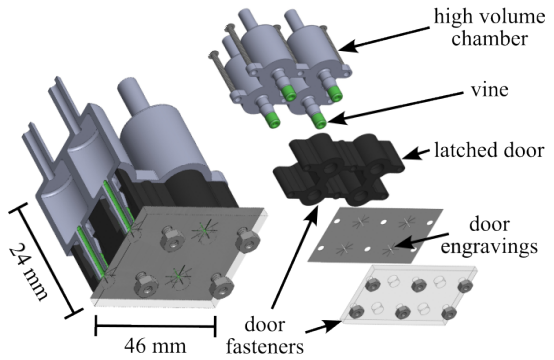

Fig. 10. Cross sectional and exploded view of the CAD model of the prototype with 4 injectors.

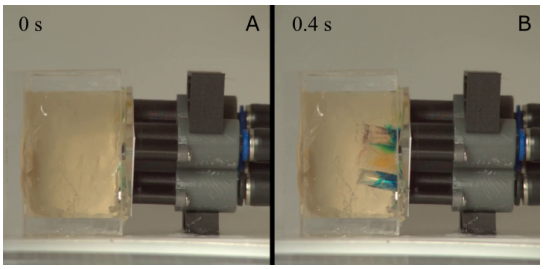

Fig. 11. High-speed injection of a vine into clear gelatin before and after latch release.

front of the vines with 3D printed fasteners. The laser-cutter engravings act as a weak point which undergo brittle fracture upon contact with high pressure vines, thus releasing the latch. Burst pressure is tuned by varying the depth and pattern of the engravings. This mechanism was inspired by spore launching of certain ascomycete fungi [23].

The entire device fits within a 46 mm x 37 mm x 24 mm volume, which is too large to serve as a wearable patch, but an appropriately scaled version would operate in a similar manner. Injections of the device array at 48 kPa successfully entered the artificial skin. Fig. 11 presents the pre- and post-injection of dye into gelatin, with visible dye diffusion.

VI. Conclusions and Future Work

The dynamic model presented here provides a means of characterizing dynamic vine speeds and positions based on factors such as geometry, material property, driving pressure, and yield pressure. This allows for prediction of vine performance prior to fabrication to enable tuning of parameters to meet target performance specifications. Future work could test model robustness for materials other than TPU, test a larger range of scales to see if scaling trends hold true, and investigate the feasibility of TDD vines on the micron-scale.

References

[1] J. P. Mascarenhas, "Molecular mechanisms of pollen tube growth and differentiation." *The Plant Cell*, vol. 5, no. 10, p. 1303, 1993.

[2] R. R. Lew, "How does a hypha grow? the biophysics of pressurized growth in fungi," *Nature Reviews Microbiology*, vol. 9, no. 7, pp. 509–518, 2011.

[3] T. Mitchison and M. Kirschner, "Cytoskeletal dynamics and nerve growth," *Neuron*, vol. 1, no. 9, pp. 761–772, 1988.

[4] E. Del Dottore, A. Mondini, N. Rowe, and B. Mazzolai, "A growing soft robot with climbing plant–inspired adaptive behaviors for navigation in unstructured environments," *Science Robotics*, vol. 9, no. 86, p. eadi5908, 2024.

[5] M. M. Hausladen, B. Zhao, M. S. Kubala, L. F. Francis, T. M. Kowalewski, and C. J. Ellison, "Synthetic growth by self-lubricated photopolymerization and extrusion inspired by plants and fungi," *Proceedings of the National Academy of Sciences*, vol. 119, no. 33, p. e2201776119, 2022.

[6] M. Kayser, L. Cai, S. Falcone, C. Bader, N. Inglessis, B. Darweesh, and N. Oxman, "Fiberbots: an autonomous swarm-based robotic system for digital fabrication of fiber-based composites," *Construction Robotics*, vol. 2, pp. 67–79, 2018.

[7] L. H. Blumenschein, A. M. Okamura, and E. W. Hawkes, "Modeling of bioinspired apical extension in a soft robot," in *Conference on Biomimetic and Biohybrid Systems*. Springer, 2017, pp. 522–531.

[8] L. H. Blumenschein, M. M. Coad, D. A. Haggerty, A. M. Okamura, and E. W. Hawkes, "Design, modeling, control, and application of everting vine robots," *Frontiers in Robotics and AI*, vol. 7, p. 548266, 2020.

[9] M. M. Coad, L. H. Blumenschein, S. Cutler, J. A. R. Zepeda, N. D. Naclerio, H. El-Hussieny, U. Mehmood, J.-H. Ryu, E. W. Hawkes, and A. M. Okamura, "Vine robots," *IEEE Robotics & Automation Magazine*, vol. 27, no. 3, pp. 120–132, 2019.

[10] N. D. Naclerio, A. Karsai, M. Murray-Cooper, Y. Ozkan-Aydin, E. Aydin, D. I. Goldman, and E. W. Hawkes, "Controlling subterranean forces enables a fast, steerable, burrowing soft robot," *Science Robotics*, vol. 6, no. 55, p. eabe2922, 2021.

[11] M. Li, R. Obregon, J. J. Heit, A. Norbash, E. W. Hawkes, and T. K. Morimoto, "Vine catheter for endovascular surgery," *IEEE Transactions on Medical Robotics and Bionics*, vol. 3, no. 2, pp. 384–391, 2021.

[12] M. Thiel, J. Norenburg, V. Häussermann, and G. Försterra, "Nemertea—ribbon worms," *Marine Benthic Fauna of Chilean Patagonia. Nature in Focus, Puerto Montt, Chile*, pp. 369–380, 2009.

[13] A. Karabulut, M. McClain, B. Rubinstein, K. Z. Sabin, S. A. McKinney, and M. C. Gibson, "The architecture and operating mechanism of a cnidarian stinging organelle," *Nature Communications*, vol. 13, no. 1, p. 3494, 2022.

[14] T. Nüchter, M. Benoit, U. Engel, S. Özbek, and T. W. Holstein, "Nanosecond-scale kinetics of nematocyst discharge," *Current Biology*, vol. 16, no. 9, pp. R316–R318, 2006.

[15] E. W. Hawkes, L. H. Blumenschein, J. D. Greer, and A. M. Okamura, "A soft robot that navigates its environment through growth," *Science Robotics*, vol. 2, no. 8, p. eaan3028, 2017.

[16] A. Ayalon, I. Shichor, Y. Tal, and T. Lotan, "Immediate topical drug delivery by natural submicron injectors," *International journal of pharmaceutics*, vol. 419, no. 1-2, pp. 147–153, 2011.

[17] R. Jitosho, N. Agharese, A. Okamura, and Z. Manchester, "A dynamics simulator for soft growing robots," in *2021 IEEE International Conference on Robotics and Automation (ICRA)*. IEEE, 2021, pp. 11 775–11 781.

[18] H. J. Qi and M. C. Boyce, "Stress–strain behavior of thermoplastic polyurethanes," *Mechanics of materials*, vol. 37.

[19] A. A. Amiri Moghadam, S. Alaie, S. Deb Nath, M. Aghasizade Shaarbaf, J. K. Min, S. Dunham, and B. Mosadegh, "Laser cutting as a rapid method for fabricating thin soft pneumatic actuators and robots," *Soft robotics*, vol. 5, no. 4, pp. 443–451, 2018.

[20] S. Divi, X. Ma, M. Ilton, R. St. Pierre, B. Eslami, S. Patek, and S. Bergbreiter, "Latch-based control of energy output in spring actuated systems," *Journal of the Royal Society Interface*, vol. 17, no. 168, p. 20200070, 2020.

[21] M. B. Brown, G. P. Martin, S. A. Jones, and F. K. Akomeah, "Dermal and transdermal drug delivery systems: current and future prospects," *Drug delivery*, vol. 13, no. 3, pp. 175–187, 2006.

[22] Y. Zhang, J. Yu, A. R. Kahkoska, J. Wang, J. B. Buse, and Z. Gu, "Advances in transdermal insulin delivery," *Advanced drug delivery reviews*, vol. 139, pp. 51–70, 2019.

[23] F. Trail, "Fungal cannons: explosive spore discharge in the ascomycota," *FEMS microbiology letters*, vol. 276, no. 1, pp. 12–18, 2007.